

Article

Two Excited State Collaboration of Heteroleptic Ir(III)-Coumarin Complexes for H₂ Evolution Dye-Sensitized Photocatalysts †

Atsushi Kobayashi * , Eiichirou Muramatsu, Masaki Yoshida and Masako Kato *

Department of Chemistry, Faculty of Science, Hokkaido University, North-10 West-8, Kita-ku, Sapporo, Hokkaido 060-0810, Japan; e36@eis.hokudai.ac.jp (E.M.); myoshida@sci.hokudai.ac.jp (M.Y.)

* Correspondence: akoba@sci.hokudai.ac.jp (A.K.); mkato@sci.hokudai.ac.jp (M.K.)

† This paper is an extended version of our paper published in: “Kobayashi, A.; Watanabe, S.; Yoshida, M.; Kato, M. Importance of the Molecular Orientation of an Ir(III)-heteroleptic Photosensitizer Immobilized on TiO₂ Nanoparticles. *ACS Appl. Energy Mater.* **2018**, *1*, 2882–2890”.

Abstract: Interfacial electron injection from a photoexcited surface-immobilized dye to a semiconductor substrate is a key reaction for dye-sensitized photocatalysts. We previously reported that the molecular orientation of heteroleptic Ir(III) photosensitizer on the TiO₂ nanoparticle surface was important for efficient interfacial electron injection. In this work, to overcome the weak light absorption ability of heteroleptic Ir(III) photosensitizer and to improve the photoinduced charge-separation efficiency at the dye–semiconductor interface, we synthesized two heteroleptic Ir(III) complexes with different coumarin dyes, [Ir(C6)₂(H₄CPbpy)]Cl and [Ir(C30)₂(H₄CPbpy)]Cl [Ir-CX; X = 6 or 30; HC6 = 3-(2-enzothiazolyl)-7-(diethylamino)coumarin, HC30 = 3-(2-*N*-methylbenzimidazolyl)-7-*N,N*-diethylaminocoumarin, H₄CPbpy = 4,4′-bis(methylphosphonic acid)-2,2′-bipyridine], as the cyclometalated ligands and immobilized them on the surface of Pt-cocatalyst-loaded TiO₂ nanoparticles. Ultraviolet-visible absorption and emission spectroscopy revealed that the singlet ligand-centered (¹LC) absorption and triplet ³LC emission bands of Ir-C30 occurred at shorter wavelengths than those of Ir-C6, while time-dependent density-functional-theory data suggested that the ligand-to-ligand charge transfer (LLCT) excited states of the two complexes were comparable. The photocatalytic H₂ evolution activity of the Ir-C6-sensitized Pt-TiO₂ nanoparticles (Ir-C6@Pt-TiO₂) under visible light irradiation ($\lambda > 420$ nm) was higher than that of Ir-C30@Pt-TiO₂. In contrast, their activities were comparable under irradiation with monochromatic light ($\lambda = 450 \pm 10$ nm), which is absorbed comparably by both Ir-CX complexes. These results suggest that the internal conversion from the higher-lying LC state to the LLCT state effectively occurs in both Ir-CX complexes to trigger electron injection to TiO₂.

Keywords: photocatalysis; water splitting; Ir(III) complex; coumarin; dye sensitization



Citation: Kobayashi, A.; Muramatsu, E.; Yoshida, M.; Kato, M. Two Excited State Collaboration of Heteroleptic Ir(III)-Coumarin Complexes for H₂ Evolution Dye-Sensitized Photocatalysts. *Energies* **2021**, *14*, 2425. <https://doi.org/10.3390/en14092425>

Academic Editor: Julien Warnan

Received: 4 March 2021

Accepted: 21 April 2021

Published: 24 April 2021

Publisher's Note: MDPI stays neutral with regard to jurisdictional claims in published maps and institutional affiliations.



Copyright: © 2021 by the authors. Licensee MDPI, Basel, Switzerland. This article is an open access article distributed under the terms and conditions of the Creative Commons Attribution (CC BY) license (<https://creativecommons.org/licenses/by/4.0/>).

1. Introduction

Following the discovery of the “Honda–Fujishima effect” [1], the photocatalytic water splitting reaction has attracted considerable attention because it produces a renewable and clean energy resource, H₂, from water under solar light irradiation without the formation of any environmental pollutants. Dye sensitization is one of the most useful and promising techniques that utilizes visible light effectively because the light absorption ability can be widely modified by surface-immobilized dye molecules [2]. Various dyes ranging from organic molecules and metal complexes to semiconductor/metal nanoparticles have been developed to date [3–5]. Among them, heteroleptic Ir(III) complexes have been extensively studied [6,7] in the fields of photocatalysis [8–26] and photovoltaics [27–31]. This is because these unique photosensitizers can generate the intramolecular charge-separated state directly by ligand-to-ligand charge-transfer (LLCT) transition. A typical example is the

$[\text{Ir}(\text{bpy})(\text{ppy})_2]^+$ complex (bpy = 2,2'-bipyridine; Hppy = 2-phenylpyridine), which shows a relatively long LLCT excited state lifetime (several hundred nanoseconds) and a suitable redox potential for water splitting [8]. Bernhard et al. reported on the high quantum yield for the H_2 production (QY = 0.26) of a homogeneous photocatalytic system composed of an $[\text{Ir}(\text{bpy})(\text{ppy})_2]^+$ photosensitizer and platinum colloids without any electron relay [10]. A highly active heterogeneous photocatalyst for H_2 evolution was also reported by Zou et al., created by the combination of Pt-loaded titanium dioxide (Pt-TiO₂) particles with the heteroleptic Ir(III) complex $\text{Ir}(4\text{-CF}_3\text{-bt})_2(\text{Hbpd})$ [4-CF₃bt = (4-trifluoromethyl)-2-phenylbenzothiazole; H₂bpd = 2,2'-bipyridine-4,4'-dicarboxylic acid] [14]. We recently discovered that the molecular orientation of an $[\text{Ir}(\text{bpy})(\text{ppy})_2]$ -type dye on the Pt-TiO₂ nanoparticle surface greatly affected the photocatalytic H_2 evolution activity because of the directional nature of the LLCT transition state [25]. However, the small molar absorption coefficient of the LLCT band of heteroleptic Ir(III) complexes severely limits their application to photovoltaics and photocatalysis.

The cyclometalation of coumarin dyes is a promising method to improve the visible light absorption abilities of heteroleptic Ir(III) complexes [32–40]. Takizawa et al. reported that the Ir(III) complex bearing two 3-(2-enzothiazolyl)-7-(diethylamino)coumarin dyes (HC6; coumarin-6) as the cyclometalated ligands, namely $[\text{Ir}(\text{C}_6)_2(\text{bpy})]^+$ (bpy = 2,2'-bipyridine) exhibited a remarkably strong ligand-centered (LC) absorption band in the visible region, and photocatalytic H_2 evolution was achieved by combination with $[\text{Co}(\text{bpy})_3]\text{Cl}_2$ as the water reduction molecular catalyst [32]. Recently, Wang et al. reported that the Ir(III)-coumarin complex with a boron dipyrromethene (BODIPY) moiety exhibited a very high H_2 evolution photocatalytic activity in the presence of the molecular catalyst $\text{Co}(\text{dmgH})_2(\text{py})\text{Cl}$ (py = pyridine, dmgH₂ = dimethylglyoxime) and sacrificial electron donor 4-dimethylaminotoluene (DMT) [40]. These studies indicate that the LC excited state localized on the coumarin ligand can improve the light absorption ability of the heteroleptic Ir(III)-coumarin complex; however, the importance of the internal conversion between the LC and LLCT states is still unclear. Furthermore, reports on Ir(III)-coumarin complexes as photosensitizing dyes for heterogeneous systems are scarce [36]. Thus, in this work, to adjust the energy difference between the LC and LLCT excited states, we synthesized two Ir(III) complexes, Ir-C6 and Ir-C30 (Figure 1), composed of HC6 or 3-(2-*N*-methylbenzimidazolyl)-7-*N,N*-diethyl aminocoumarin (HC30; coumarin 30) dyes and immobilized them on the Pt-TiO₂ surface by using the phosphonate anchors of the CPbpy ligand [H₄CPbpy = 4,4'-bis(methylphosphonic acid)-2,2'-bipyridine]. The ligand replacement from C6 to C30 provides further insight into the importance of the energy difference between the LLCT and LC states for photo-induced electron injection to TiO₂. Herein, we report on the photophysical properties of Ir-CX and photocatalytic H_2 evolution reactions driven by nanoparticle photocatalysts composed of Ir-CX-immobilized Pt-TiO₂ nanoparticles (Ir-CX@Pt-TiO₂, X = 6, 30). Using time-dependent density-functional-theory (TD-DFT) calculations, we demonstrated that the photocatalytic H_2 evolution activity of Ir-C6@Pt-TiO₂ under visible-light irradiation ($\lambda > 420$ nm) was remarkably higher than that of Ir-C30@Pt-TiO₂, while the apparent quantum yield (AQY) of H_2 evolution under monochromatic light irradiation ($\lambda = 450 \pm 10$ nm) was comparable (AQY \cong 2%), probably because of the comparable LLCT transition states of both Ir-CX complexes.

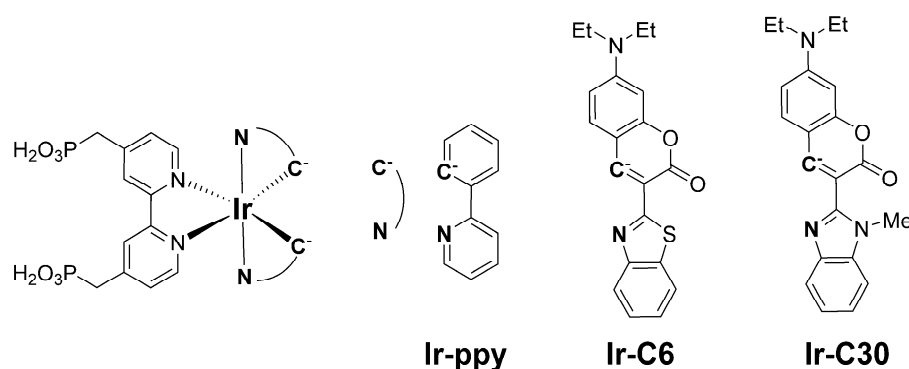


Figure 1. Molecular structures of the Ir(III) complexes $[\text{Ir}(\text{ppy})_2(\text{H}_4\text{CPbpy})]^+$ (Ir-ppy), $[\text{Ir}(\text{C6})_2(\text{H}_4\text{CPbpy})]^+$ (Ir-C6), and $[\text{Ir}(\text{C30})_2(\text{H}_4\text{CPbpy})]^+$ (Ir-C30).

2. Materials and Methods

2.1. Syntheses

Caution! Although we did not encounter any difficulties, most of the chemicals used in this study are potentially harmful and should be used in small quantities and handled with care in a fume hood. All commercially available starting materials, including the coumarin dyes (HC6 and HC30), were used as received without further purification. The TiO_2 nanoparticles (SSP-25, anatase, diameter: ~ 9 nm) were purchased from Sakai Chemical Industry Co. Ltd., Osaka, Japan, Pt- TiO_2 (Pt: 2.5 wt%, ~ 2.4 nm in diameter) was prepared using a previously reported photodeposition method [41] and characterized by powder X-ray diffraction (PXRD) and transmission electron microscope (TEM) measurements (Figure S1). The dichloride-bridged Ir(III) complexes $[\text{Ir}(\text{C6})_2\text{Cl}]_2$ and $[\text{Ir}(\text{C30})_2\text{Cl}]_2$ and the H_4CPbpy ligand were prepared according to methods reported in the literature [42,43].

2.1.1. Synthesis of $[\text{Ir}(\text{C6})_2(\text{H}_4\text{CPbpy})]\text{Cl}$ (Ir-C6)

$[\text{Ir}(\text{C6})_2\text{Cl}]_2$ (75.5 mg, 40.7 μmol) and H_4CPbpy (28.8 mg, 83.7 μmol) were added to 18 mL THF/ H_2O mixture (1:1 *v/v*) in a capped vial. The mixture was heated at 130 $^\circ\text{C}$ for 20 min under microwave irradiation (Biotage Initiator⁺). The reaction mixture was cooled naturally to room temperature (293 K) and then filtered. Approximately 130 mL of CH_3CN was added to the filtrate, which was then incubated for 3 d at 298 K to afford the target complex Ir-C6 as yellow crystals. Yield: 50.3 mg (40.7 μmol , 49%). ^1H NMR (400 MHz, THF- d^8 / D_2O +NaOD = 1/1 *v/v*, δ ppm): 8.51 (s, 2H), 8.44 (d, 2H), 7.97 (d, 2H), 7.73 (d, 2H), 7.33 (t, 2H), 7.15 (t, 2H), 6.45 (s, 2H), 6.12 (dd, 2H), 5.95 (d, 2H), 5.77 (d, 2H), 3.31–3.36 (m, 12H), 1.06 (t, 12H). Anal. Calcd. (%) for $\text{C}_{52}\text{H}_{48}\text{ClIrN}_6\text{O}_{10}\text{P}_2\text{S}_2 \cdot 3\text{H}_2\text{O}$: C, 47.15; H, 4.11; N, 6.34. Found: C, 46.98; H, 3.62; N, 6.33.

2.1.2. Synthesis of $[\text{Ir}(\text{C30})_2(\text{H}_4\text{CPbpy})]\text{Cl}$ (Ir-C30)

$[\text{Ir}(\text{C30})_2\text{Cl}]_2$ (82.2 mg, 44.7 μmol) and H_4CPbpy (30.4 mg, 88.3 μmol) were added to 18 mL THF/ H_2O mixture (1:1 *v/v*) in a capped vial. The mixture was heated at 130 $^\circ\text{C}$ for 20 min under microwave irradiation (Biotage Initiator⁺). The reaction mixture was cooled naturally to room temperature and then filtered. Approximately 130 mL of CH_3CN was added to the filtrate, which was then incubated for 3 d at 298 K to afford the target complex Ir-C30 as yellow crystals. Yield: 37.0 mg (30.1 μmol , 34%). ^1H NMR (400 MHz, THF- d^8 : D_2O = 1:1 *v/v*, δ ppm): 8.28 (s, 2H), 8.18 (d, 2H), 7.55–7.59 (m, 4H), 7.25 (t, 2H), 6.91 (t, 2H), 6.65 (d, 2H), 6.38 (d, 2H), 5.95 (dd, 2H), 5.50 (d, 2H), 4.31 (s, 6H), 3.29–3.36 (m, 8H), 3.06 (d, 4H), 1.06 (t, 12H). Anal. Calcd. (%) for $\text{C}_{54}\text{H}_{54}\text{ClIrN}_8\text{O}_{10}\text{P}_2 \cdot 4\text{H}_2\text{O}$: C, 48.52; H, 4.67; N, 8.38. Found: C, 48.30; H, 4.11; N, 8.39.

2.1.3. Preparation of the Nanoparticle Photocatalysts (Ir-CX@Pt- TiO_2)

The nanoparticle photocatalyst Ir-ppy@Pt- TiO_2 was prepared according to our previously reported method [25,44]. The other two photocatalysts, Ir-C6@Pt- TiO_2 and Ir-C30@Pt-

TiO₂, were prepared by a similar method with minor modifications as follows: Ir-C6 or Ir-C30 (40.4 or 41.5 μmol) was dissolved in a basic THF/H₂O (73 mL) or MeOH/H₂O (36 mL) mixed solvent (1:1 *v/v* for immobilization of Ir-C6 and Ir-C30, respectively) by adding a 1 M NaOH aqueous solution (pH 11). Next, Pt-TiO₂ nanoparticle powder (50.0 mg) was added to the Ir-C6 or Ir-C30 solution and stirred continuously for 3 d in the dark. The afforded Ir(III)-photosensitizer-immobilized Pt-TiO₂ nanoparticles (Ir-C6@Pt-TiO₂ or Ir-C30@Pt-TiO₂, respectively) were collected by ultracentrifugation (50,000 rpm; 15 min) and the supernatant solution was manually removed by using a pipette. After washing twice with ~6 mL of the same mixed solvent used for immobilization (1:1 *v/v*) without basification and deionized water, the product was dried in vacuo at 298 K for 1 d. The amount of Ir(III) photosensitizer immobilized on the Pt-TiO₂ nanoparticle surface was estimated by X-ray fluorescence (XRF) and ultraviolet-visible (UV-vis) absorption spectroscopy of the supernatant solution (Figure S2, Table S1, and the “Calculation of the amount of immobilized Ir(III) complexes on the Pt-TiO₂ nanoparticles” section in the ESI).

2.2. Measurements

2.2.1. Characterization

Elemental analysis was performed using a CE-440 element analyzer at the Analysis Center, Hokkaido University. ¹H NMR spectra were recorded on a JEOL JNM-ECZ400S NMR spectrometer at room temperature, while energy-dispersive XRF spectra were recorded on a Bruker S2 PUMA analyzer using a Pd target. Dynamic light scattering (DLS) analysis was conducted using an OTSUKA ELSZ-1000SCI analyzer. IR spectra were recorded on a JASCO FT-IR 660 spectrophotometer using the KBr method. PXRD measurements were conducted using a Bruker D8 Advance diffractometer equipped with a graphite monochromator using Cu-Kα radiation. The single-crystal X-ray diffraction (SXRD) data of Ir-C30 were collected using a Rigaku XtaLAB synergy diffractometer equipped with Cu-Kα radiation [PhotonJet(Cu)]. A suitable crystal was mounted on a MicroMount using paraffin oil. The crystal was then cooled using an N₂-flow-type temperature controller, and the diffraction data were processed using CrysAlisPRO software [45]. The structures were solved by the direct method and refined by full-matrix least-squares refinement using SHELXL [46]. The non-hydrogen atoms were refined anisotropically, while the hydrogen atoms were refined using the riding model. All calculations were performed using the Olex2 software package [47]. The crystallographic data and selected bond lengths and angles are listed in Tables S2 and S3 in the Supporting Information. Full crystallographic data were deposited with the Cambridge Crystallographic Data Center (CCDC-2062083).

2.2.2. Photophysical and Electrochemical Measurements

UV-vis absorption and luminescence spectra were recorded on a Shimadzu UV-2400PC spectrophotometer and JASCO FP-8600 spectrofluorometer, respectively. Quartz cells with a 1 cm optical path length were used for both spectroscopic analyses in the solution state. Prior to the luminescence measurements, the sample solutions were degassed by N₂ bubbling for 15 min. The emission quantum yields (Φ_{em}) were measured using a Hamamatsu C9920-02 absolute photoluminescence quantum yield measurement system equipped with an integrating sphere apparatus and a 150 W continuous-wave xenon light source. Emission lifetime measurements were conducted using a Hamamatsu Photonics C4334 system equipped with a streak camera as the photodetector and a nitrogen laser as the excitation light source ($\lambda_{ex} = 337$ nm).

Cyclic voltammetry (CV) was performed using a HOKUTO DENKO HZ-3000 electrochemical measurement system equipped with Pt wire and Ag/Ag⁺ electrodes as the counter and reference electrodes, respectively. An Ir(III) complex-modified indium tin oxide (ITO) electrode was used as the working electrode. The ITO electrode was prepared according to a slightly modified literature method [48] as follows: A bare ITO electrode was cleaned by heating in basic hydrogen peroxide solution for 30 min at 80 °C and then washed with deionized water. Next, the pre-cleaned ITO electrode was immersed in a

0.1 mM THF/H₂O (1:1 *v/v*) solution of Ir-C6 or MeOH/H₂O (1:1 *v/v*) solution of Ir-C30 for 1 d at room temperature. Subsequently, the electrode was washed with THF/H₂O (1:1 *v/v*) or MeOH/H₂O (1:1 *v/v*) and dried under reduced pressure. A CH₃CN solution containing 0.1 M tetrabutylammonium hexafluorophosphate (TBAPF₆) as the supporting electrolyte was deaerated by N₂ bubbling for 15 min and subsequently used in the CV experiments.

2.3. Photocatalytic Hydrogen Evolution Reactions

For the photochemical H₂ evolution reactions, each sample was prepared using a hand-made Schlenk-flask-equipped quartz cell (volume: 257 mL). A typical sample preparation was as follows: Ir(III)-photosensitizer-immobilized Pt-TiO₂ nanoparticles and *L*-ascorbic acid (AA) were added to the quartz cell as the photocatalyst and sacrificial electron donor (SED), respectively. The total sample volume was adjusted to 10 mL by adding a CH₃CN/deionized water (1:1 *v/v*) mixture. Each sample flask was doubly sealed using rubber septa and degassed by Ar bubbling for 1 h. Prior to irradiation, the gas (0.3 mL) was collected from the headspace using a gas-tight syringe (Hamilton 1001LTN) and analyzed by gas chromatography (GC, Shimadzu GC-14B) to confirm Ar purging. Subsequently, the samples were irradiated using a 300 W xenon lamp (MAX-303, ASAHI Spectra) in a water bath (293 K) combined with a visible-light-passed mirror module (385 nm < λ < 740 nm) and a longpass (SCF-50S-42L, λ > 420 nm) or band-pass (HMX0450, λ = 450 ± 10 nm) filter at room temperature. The gas samples (0.3 mL) were collected from the headspace at each analysis time (15 or 60 min) to determine the amount of H₂ evolved as a function of irradiation time. The AQY (Φ) was calculated using the equation:

$$\Phi = N_e/N_p = 2N_{\text{H}_2}/N_p \quad (1)$$

where N_e represents the number of reacted electrons, N_{H_2} is the number of evolved H₂ molecules, and N_p is the number of incident photons.

2.4. Theoretical Calculations

TD-DFT calculations were performed using the CAM-B3LYP functional with SDD(Ir) and 6-31+G** (other atoms) basis sets using Gaussian 09W [49–52]. Geometry optimization was achieved using the B3LYP functional and the same basis sets [53]. In these calculations, the Et₂N-group of the coumarin ligand was replaced by the Me₂N-group and the two methylenephosphonate groups attached to the H₄CPbpy ligand were replaced by H atoms to reduce the calculation cost. The Cartesian coordinates of the optimized structures are listed in Table S4 in the supporting information. Molecular orbital (MO) diagrams for all the complexes were reproduced using GaussView 5.0 (Wallingford, CT, USA) [54].

3. Results and Discussion

3.1. Molecular Structure of Ir-C30

Figure 2 shows the molecular structure of Ir-C30 determined by SXRD analysis.

The Ir(III) center was surrounded by two cyclometalated C30 ligands and one CPbpy ligand to form the octahedral IrC₂N₄ coordination geometry. The coordinating C atoms of the C30 ligands were located at the *trans* positions to the N atoms of the CPbpy ligand, as observed for the heteroleptic Ir(III) cyclometalated complexes. The N–Ir–C bond angles of the C30 ligand in Ir-C30 (~79°) were near-identical to those of the C6 ligand in [Ir(C6)₂(vacac)] (~80°, vacac = allylacetate) reported by DeRosa et al. [55], suggesting that the effect of functional group substitution, from the thiazole to methylimidazole ring, on the Ir(III) coordination environment was negligible (Table S3). In contrast, the torsion angle between the coumarin ring and thiazole/methyl-imidazole ring was notable. Indeed, these two rings were located in almost the same plane in [Ir(C6)₂(vacac)], while the methyl-imidazole ring was largely twisted against the coumarin ring with a torsion angle ranging between 23 and 27°, probably because of the steric repulsion between the methyl group attached to the imidazole ring and the carbonyl group of the coumarin ring.

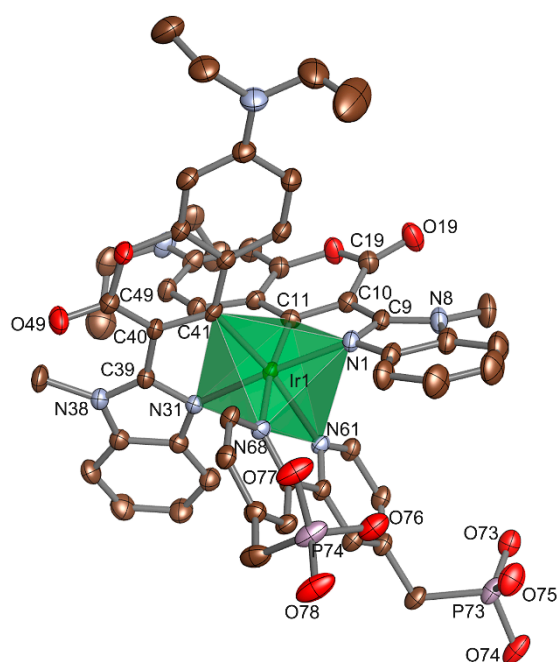


Figure 2. Molecular structure of Ir-C30. Ir(III) coordination sphere is depicted as a green octahedron. Brown, light blue, red, and pale pink ellipsoids represent C, N, O, and P atoms, respectively, and H atoms are omitted for clarity. Displacement parameters are drawn at the 50% probability level.

3.2. Photophysical and Electrochemical Properties

To reveal the role of the coumarin ligand on the photophysical properties of the Ir(III) cyclometalated complexes, the UV-vis absorption and luminescence spectra of Ir-C6 and Ir-C30 were obtained in the solution state at 298 K (Figure 3).

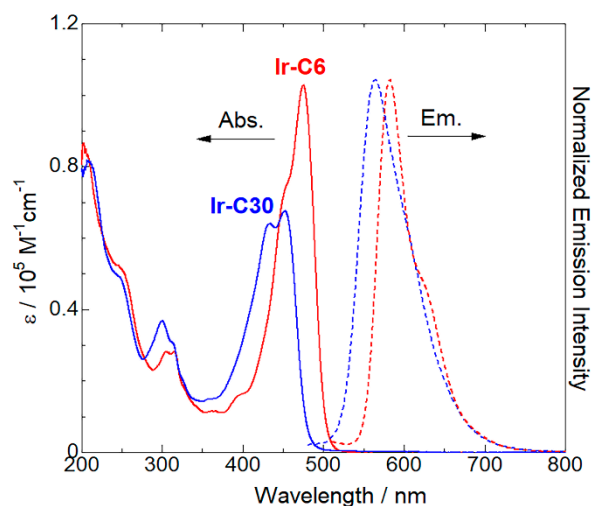


Figure 3. Ultraviolet-visible absorption (solid lines) and luminescence (dotted lines; $\lambda_{\text{ex}} = 450$ and 475 nm) spectra of Ir-C30 and Ir-C6 in MeOH/H₂O solution (1:1 v/v, pH = 11) at 298 K.

As already reported by several groups, the Ir(III) complex $[\text{Ir}(\text{C}6)_2(\text{bpy})]^+$ without the methylenephosphonic acid linkers exhibited a strong absorption band at 483 nm, which originated from the LC transition in the C6 ligand coupled with the metal-ligand-to-ligand charge transfer (MLLCT) transition [32,40]. The two Ir(III) complexes Ir-C6 and Ir-C30, with two phosphonic acid linkers, also exhibited similar absorption and emission bands in the visible region. The absorption and emission bands observed for Ir-C6 were slightly shifted to shorter wavelengths (~8 nm) than those of $[\text{Ir}(\text{C}6)_2(\text{bpy})]^+$ (Table 1),

attributed to the electron-donating effect of the $-\text{CH}_2\text{-PO}_3\text{H}_2$ linker attached to the bpy ligand. The absorption and emission bands observed for Ir-C30 were located at a shorter (by ~ 20 nm) wavelength than those of Ir-C6. Considering that the thiazole ring in C6 was replaced by the methyl imidazole ring in the C30 ligand, the spectral difference between Ir-C6 and Ir-C30 was assigned to the difference in the electron-donating ability of these functional groups. Indeed, the methyl-imidazole ring is generally electron-poorer than the thiazole group because of the higher electronegativity of the N atom over that of S, leading to a higher LC transition energy for Ir-C30 over that for Ir-C6.

Table 1. Comparison of the photophysical and electrochemical data of Ir-C30, Ir-C6, and Ir-ppy.

Complex	λ_{abs} (ϵ) /nm	λ_{em} ^a /nm	τ_{em} ^b / μs	Φ ^c	k_{r} ^d / s^{-1}	k_{nr} ^e / s^{-1}	E_{ox}^f /V vs. NHE	E_{ox}^{*g} /V vs. NHE	Ref.
Ir-C30	452 (6.76×10^4)	564	7.03	0.10	1.5×10^4	1.3×10^5	+1.34	−0.86	This work
Ir-C6	475 (10.3×10^4)	582	19.2	0.39	2.1×10^4	3.2×10^4	+1.41	−0.72	This work
Ir-ppy	464 (6.1×10^2)	587	0.29	0.10	3.5×10^5	3.1×10^6	+1.67	−0.63	[25]

^a Emission maximum; ^b Emission lifetime; ^c Photoluminescence quantum yield. ^d Radiative rate constants (k_{r}) were estimated from Φ/τ_{em} .

^e Nonradiative rate constants (k_{nr}) were estimated from $k_{\text{r}}(1 - \Phi)/\Phi$. ^f Estimated by CV measurements (Figure S5). ^g E_{ox}^* was estimated using the equation $E_{\text{ox}}^* = E_{\text{ox}} - E_{00}$, where E_{00} was approximated as λ_{em} .

This trend agrees well with that observed for the UV-vis absorption spectra of the C6 and C30 ligands in solution (Figure S3 and Table S5). The lowest-energy absorption band of C30 was located at a shorter (by ~ 44 nm) wavelength than that of C6. Moreover, a marked difference was also observed in the emission lifetime and quantum yield: The emission lifetime of Ir-C30 was less than half that of Ir-C6 (Figure S4), while the emission quantum yield of Ir-C30 at 298 K in the solution state was approximately one-fourth that of Ir-C6 (Table 1). As a result, the non-radiative rate constant (k_{nr}) of Ir-C30 was estimated to be approximately four times higher than that of Ir-C6, while the radiative rate constants (k_{r}) of the two complexes were comparable. These results indicate that the functional group difference in the coumarin ligand exerted considerable effects not only on the emission wavelength but also on the deactivation process from the photo-excited state. The faster non-radiative deactivation of Ir-C30 over that of Ir-C6 was attributed to the structural distortion around the C30 ligand, as discussed in Section 3.1. This non-planar structure of the C30 ligand may stabilize the non-radiative metal-centered (d–d) excited state. This is also consistent with the electrochemical measurements, wherein the quasi-reversible Ir(IV)/Ir(III) redox wave was observed at +1.34 V (vs. NHE, Figure S5) for Ir-C30, which was slightly less positive than that of Ir-C6 (+1.41 V). This was probably due to the weaker ligand field splitting of the C30 ligand over that of C6. On the other hand, the emission lifetimes of both Ir(III)-coumarin complexes were at least one order of magnitude longer than that of the simple cyclometalated complex Ir-ppy. Furthermore, the redox potentials at the photo-excited state Ir(IV)/Ir(III)* of Ir-CX were estimated to be slightly more negative than that of Ir-ppy (E_{ox}^* in Table 1), suggesting the potential of these two Ir-CX complexes as photosensitizers for the H_2 evolution reaction.

To obtain further insight into the differences between Ir-C6 and Ir-C30, TD-DFT calculations were conducted for the simplified Ir-C6' and Ir-C30' complexes, where the $-\text{CH}_2\text{PO}_3\text{H}_2$ groups attached to the bpy ligand and the diethylamino group of the coumarin (C6 and C30) ligands were replaced by H atoms and the dimethylamino group, respectively. The bond lengths around the central Ir(III) cation in the optimized Ir-C6' and Ir-C30' structures are reasonably comparable to those observed in the X-ray structure of Ir-C30 (Table S6). In the optimized structures, the planarity of the coumarin ligands was notably different, as discussed in Section 3.1. The dihedral angle between the coumarin and methyl imidazole rings was estimated to be 18.4° for Ir-C30' and near-zero for Ir-C6'. Considering

that the C6 ligand in the $[\text{Ir}(\text{C}_6)_2(\text{vacac})]$ complex was also near-planar, the non-planarity of the C30 ligand was attributed to the steric effect of the methyl group attached to the imidazole ring. A schematic energy diagram estimated by TD-DFT calculations is shown in Figure 4, while the estimated transition energy and oscillator strength of each transition are listed in Tables S7 and S8. The highest occupied molecular orbital (HOMO) and lowest unoccupied molecular orbital (LUMO) of Ir-C6' were localized on the π and π^* orbitals of C6 and the bpy ligands, respectively.

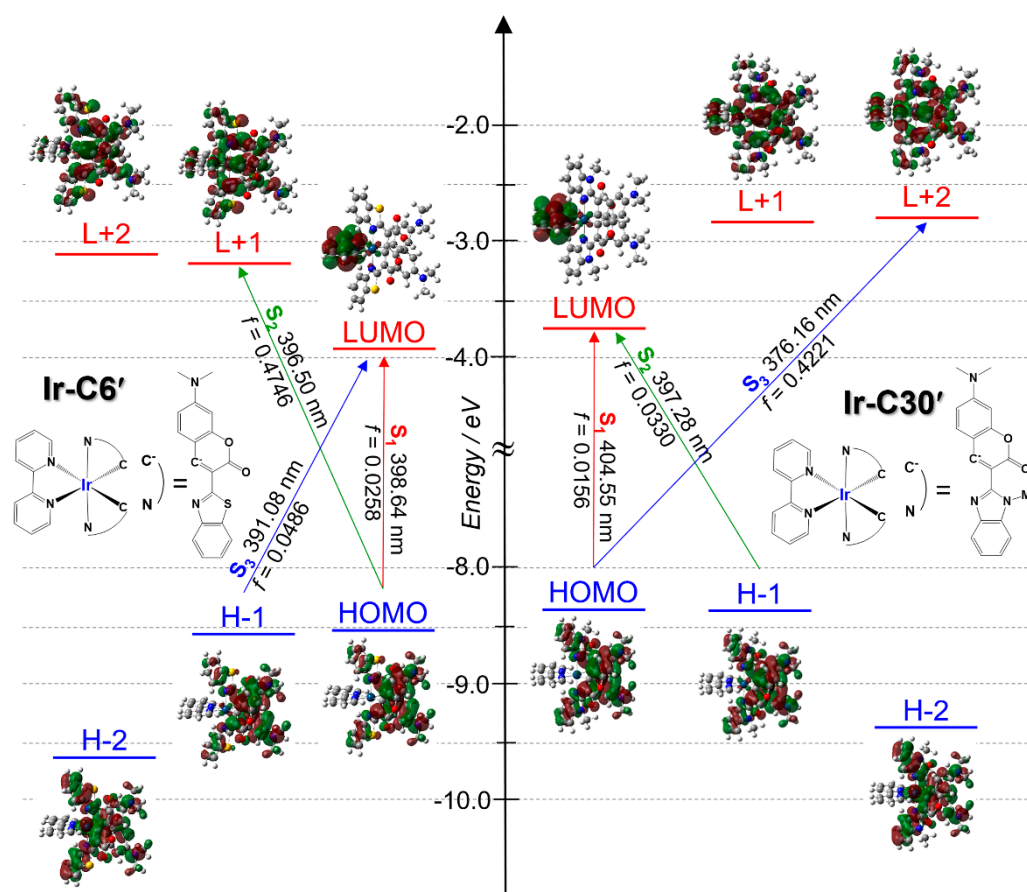


Figure 4. Schematic energy diagram and molecular orbital shapes of the simplified Ir(III)-coumarin complexes, Ir-C6' and Ir-C30', estimated by time-dependent density-functional-theory (TD-DFT) calculation. Red, green, and blue arrows schematically indicate the primary contribution for the spin-allowed first, second, and third lowest-energy electronic transitions (S_0 to S_1 , S_2 , and S_3 , respectively). The wavelength and oscillator strength of each transition are also shown.

The second and third HOMOs (H-1 and H-2, respectively) and second and third LUMOs (L+1 and L+2, respectively) were assigned to the π and π^* orbitals of the C6 ligand. These results are consistent with the results reported by several groups [37,40]. Although a similar trend was confirmed for Ir-C30', the orbital energies were positively shifted, probably due to the poorer electron-donating ability of C30 over that of C6. The positive shift of the HOMO is consistent with the negative shift of the Ir(IV)/Ir(III) redox potential observed in the CV measurements (Table 1). TD-DFT calculations also suggest a notable difference between these two complexes. The spin-allowed lowest-energy electronic (S_0 to S_1) transition was suggested to be an LLCT (from CX to bpy) transition from the HOMO to LUMO in both complexes (as indicated by the red arrows in Figure 4). The estimated transition energy was comparable (~ 400 nm) for both complexes and the oscillator strength was commonly small ($f < 0.03$, Tables S7 and S8), probably because of the small orbital overlap of these MOs. The second lowest-energy (S_0 to S_2) transition for Ir-C6' was assignable to the LC transition in the C6 ligand (HOMO to L+1, 396 nm) with a large

oscillator strength ($f = 0.48$), and the transition energy difference between the LC and LLCT transitions was negligible. In contrast, the same LC transition for Ir-C30' appeared as the third-lowest energy transition with a higher transition energy (S_3 , HOMO to L+2, 376 nm), resulting in an energy difference between the LLCT and LC transition states. The estimated LC transition energy difference between Ir-C30' and Ir-C6' (~20 nm) qualitatively agreed with the positions of the LC transition bands observed in the UV-vis absorption and emission spectra of Ir-CX (Figure 3). Notably, the lowest excited triplet state in both complexes was suggested to be in the 3LC state for both complexes, and the 3LLCT was found to be the fourth-lowest (T_4) excited state with an excitation energy similar to that of the 1LLCT state (Tables S7 and S8). Thus, these TD-DFT calculations suggest that the coumarin ligand replacement, from C6 to C30, does not affect the LLCT excited state of the Ir-CX complex but affects the LC excited state.

3.3. Synthesis and Characterization of the Ir-PS-Immobilized Pt-TiO₂ Nanoparticles

The immobilization of the Ir-C6 and Ir-C30 complexes on the Pt-TiO₂ nanoparticle surface was conducted in basified THF/H₂O and MeOH/H₂O (1:1 v/v), respectively (Experimental Section). Almost the same immobilization procedure used for Ir-ppy was applicable to Ir-C30 [25] but not to Ir-C6, probably because of the low solubility of the latter. The UV-vis absorption spectra of the supernatant solutions isolated from the immobilization reaction enabled us to estimate the amount of these immobilized Ir(III) complexes (ESI and Figure S2). The obtained results are summarized and compared to those of Ir-ppy in Table 2. The amounts of immobilized Ir-C6 and Ir-C30 were comparable (~130 nmol/1 mg TiO₂) and slightly lower than our previously reported value for Ir-ppy [25]. The surface coverage and molecular footprint (i.e., area occupied by one Ir(III) complex molecule) were calculated assuming that the TiO₂ nanoparticles were spherical with a diameter of 9 nm (ESI). The Ir-CX molecular footprint was estimated to be ~2.1 nm², which is slightly larger than that of the Ir-ppy complex. These results are reasonable because Ir-CX complexes have larger coumarin dyes as the cyclometalated ligands than the ppy ligand in Ir-ppy (Figure 1). Notably, the estimated molecular footprint based on the UV-vis absorption spectra of the supernatant solution qualitatively agreed with the value estimated from the X-ray structure of Ir-C30 (~2.2 nm², Figure S6), suggesting that the Pt-TiO₂ nanoparticle surface was almost fully covered by the Ir-CX complexes. Further evidence of Ir-CX immobilization on the Pt-TiO₂ nanoparticle surface was obtained by XRF spectroscopy (Figure 5). The characteristic peaks assigned to the Ir-L and Pt-L radiation originating from the surface-immobilized Ir-CX and Pt cocatalyst were observed clearly for both nanoparticles. The comparable peak intensities of the Ir L radiation of Ir-C30@Pt-TiO₂ and Ir-C6@Pt-TiO₂ provide further evidence that the amount of Ir-CX immobilized on the Pt-TiO₂ surface of the two nanoparticles was near-identical. The comparable intensity of the Pt-L radiation for both nanoparticles also indicates that the Pt cocatalyst loaded on the TiO₂ surface was barely detached during the Ir-CX immobilization reaction. The Ir-CX photoluminescence was negligible for both Ir-CX@Pt-TiO₂ nanoparticles in the solid state at 293 K, suggesting electron transfer quenching from the photoexcited Ir-CX* to TiO₂.

Table 2. Comparison of the immobilized amounts, surface coverage, and molecular footprints of Ir-C6, Ir-C30, and Ir-ppy.

Photocatalyst	Amount of Immobilized Ir(III) Complex (nmol/1 mg TiO ₂) ^a	Surface Coverage (nmol/cm ²)	Molecular Footprint of Ir(III) Complex (nm ²)
Ir-C6@Pt-TiO ₂	130	7.61×10^{-2}	2.17
Ir-C30@Pt-TiO ₂	137	8.10×10^{-2}	2.08
Ir-ppy@Pt-TiO ₂ ^b	175	10.5×10^{-2}	1.62

^a Estimated based on the absorbance in the UV-vis spectra of each supernatant solution (Figure S2). ^b Ref. [25].

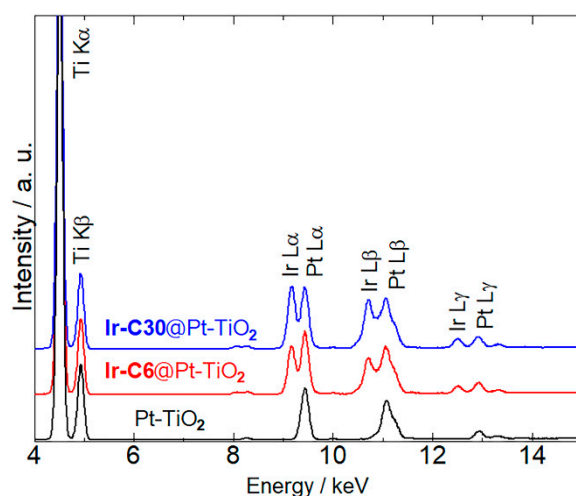


Figure 5. X-ray fluorescence (XRF) spectra of Pt-TiO₂ (black), Ir-C6@Pt-TiO₂ (red), and Ir-C30@Pt-TiO₂ (blue) in the solid state at 293 K. The intensity of each spectrum was normalized based on the Ti K. β peak at 4.93 keV.

3.4. Photocatalytic H₂ Evolution Reactions

The results of the photocatalytic H₂ evolution reactions driven by the Ir(III)-coumarin-dye-immobilized Pt-TiO₂ nanoparticles, Ir-C6@Pt-TiO₂ or Ir-C30@Pt-TiO₂, in the presence of a sacrificial AA donor aqueous solution under visible light irradiation ($\lambda > 420$ nm) are shown in Figure 6a. The amount of evolved H₂, turnover number (TON), and turnover frequency (TOF) per Ir(III) dye are listed in Table 3. In 0.2 M AA solution, both nanoparticle photocatalysts were highly active, with estimated TOFs of ~1299 and 699 for Ir-C6@Pt-TiO₂ and Ir-C30@Pt-TiO₂, respectively, which are at least two orders of magnitude larger than that of the previously reported Ir-ppy@Pt-TiO₂ under near-identical conditions.

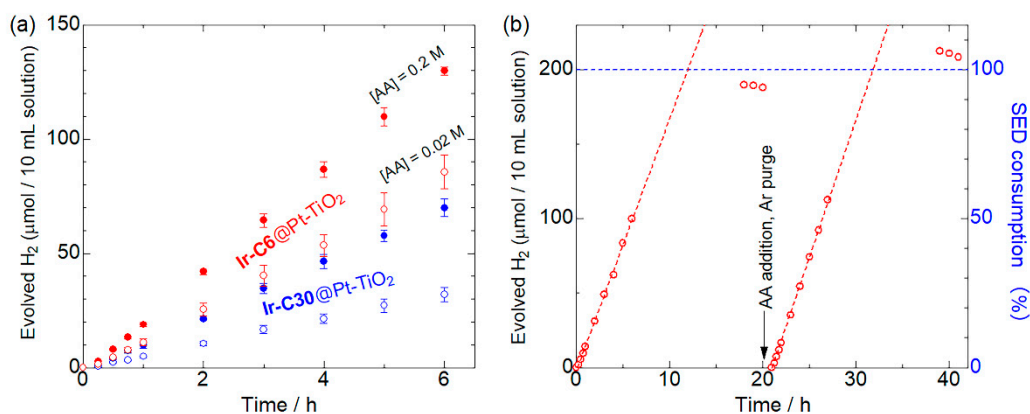


Figure 6. (a) Photocatalytic H₂ evolution reaction driven by the Pt-cocatalyst-loaded TiO₂ nanoparticles Ir-C6@Pt-TiO₂ (red) and Ir-C30@Pt-TiO₂ (blue) in 0.2 M (closed circles) and 0.02 M (open circles) L-ascorbic acid (AA) solution ([Ir] = 10 μM, pH = 4.5, CH₃CN:H₂O = 1:1 v/v) under Ar atmosphere. (b) Two-cycle photocatalytic H₂ evolution reaction driven by Ir-C6@Pt-TiO₂ in 0.02 M AA solution ([Ir] = 10 μM, pH = 4.5, CH₃CN:H₂O = 1:1 v/v) under Ar atmosphere. After the first reaction for 20 h, the AA solution was added to adjust the concentration to 0.02 M, after which the reaction solution was degassed by Ar bubbling for 1 h before the second irradiation. A 300 W xenon lamp (0.25 W) with a longpass filter ($\lambda > 420$ nm) was used as the irradiation source.

Table 3. Results of the photocatalytic H₂ evolution reactions in the presence of *L*-ascorbic acid (AA).

Photocatalyst	[Ir] (μM)	[AA] (M)	λ_{irr} (nm)	H ₂ (μmol) ^a	TON ^{a,b}	TOF ^b	Ref.
Ir-C6@Pt-TiO ₂	10	0.2	420 – 740	130	1299	217	
Ir-C6@Pt-TiO ₂	10	0.02	420 – 740	85.6	856	143	
Ir-C6@Pt-TiO ₂	40	0.2	450 \pm 10	9.33	23.3	3.89	
Ir-C30@Pt-TiO ₂	10	0.2	420 – 740	69.9	699	117	
Ir-C30@Pt-TiO ₂	10	0.02	420 – 740	32.0	320	53.3	
Ir-C30@Pt-TiO ₂	40	0.2	450 \pm 10	8.66	21.7	3.61	
Ir-ppy@Pt-TiO ₂	40	0.2	420 – 740	15.6	39	6.5	[25]

^a After 6 h of irradiation. ^b Turnover number (TON, after 6 h irradiation) and turnover frequency (TOF, per 1 h on average) were calculated based on the Ir(III) photosensitizer.

The higher activities of Ir-CX@Pt-TiO₂ indicate that the strong light adsorption ability originating from the coumarin ligand contributes to the photocatalytic H₂ evolution reaction. The TON after 6 h irradiation of Ir-C6@Pt-TiO₂ was estimated to be 1.85 times higher than that of Ir-C30@Pt-TiO₂. Considering that a constant amount of Ir(III)-coumarin complex ([Ir] = 10 μM) was used in these reactions, the higher photocatalytic activity of Ir-C6@Pt-TiO₂ under these conditions were ascribed to the wider and stronger absorption bands of Ir-C6 compared to those of Ir-C30 (Figure 3). In fact, the integral of the molar absorption coefficient of Ir-C6 in the irradiated wavelength range (>420 nm) was 1.62 times larger than that of Ir-C30. Further, the photocatalytic H₂ evolution activities of these two nanoparticles under monochromatic light irradiation ($\lambda = 450 \pm 10$ nm) were near-similar (Figure S7) because of the comparable molar absorption coefficients at 450 nm (ϵ at 450 nm = 7.13×10^4 and 6.72×10^4 for Ir-C6 and Ir-C30, respectively). Although the evolved amount of H₂ under the monochromatic light irradiation was significantly lower because of the lower number of irradiated photons, the AQYs for H₂ evolution under these conditions were estimated to be 2.3 and 2.1% for Ir-C6@Pt-TiO₂ and Ir-C30@Pt-TiO₂, respectively. These values are nearly double that of RuCP²@Pt-TiO₂ (1.4%, RuCP² = [Ru(bpy)₂(CPbpy)]²⁻, bpy = 2,2'-bipyridine), which is composed of well-known tris-bipyridyl-type Ru(II) dyes and Pt-TiO₂ nanoparticles [44]. These results suggest a superior performance of the Ir(III) heteroleptic photosensitizer for photoinduced charge separation. The comparable AQY values for Ir-CX@Pt-TiO₂ are reasonable because of the comparable driving force for electron injection to TiO₂ from the LLCT excited state, as suggested by the TD-DFT data. On the other hand, the difference in the H₂ evolution photocatalytic activity between these two nanoparticles became more pronounced in the more diluted (20 mM) AA aqueous solution. Indeed, the TON of Ir-C6@Pt-TiO₂ in 0.02 M AA solution was 856, which is 2.65 times higher than that of Ir-C30@Pt-TiO₂. This different dependence on the AA concentration suggests that the reactivity between the surface-immobilized Ir-C30 and AA is lower than that of Ir-C6. As discussed in Section 3.2, the HOMOs of both complexes are almost localized on the coumarin ligands (Figure 4). The two coumarin ligands, C6 and C30, have very similar molecular structures; however, the methyl group attached to the N atom of the C30 ligand may suppress electron donation from AA by the steric effect. In addition, as shown in Figure 7, the Ir(IV)/Ir(III) redox potential of Ir-C30 (1.34 V vs. NHE) was slightly more negative than that of Ir-C6 (1.41 V vs. NHE), suggesting a smaller driving force for electron donation from AA to the photooxidized Ir(IV) species. It should be noted that the Ir(IV)/Ir(III)* redox potentials estimated by the combination of cyclic voltammograms and emission spectra (E^*_{ox} in Table 1) may be underestimated because the higher-lying and non-emissive ³LLCT state than the emissive ³LC state could contribute to the photo-induced electron injection. Unfortunately, the emission quenching experiments to evaluate the reactivity between the photoexcited Ir-CX* and AA failed because of the very weak emission intensity at pH 4.5 condition (Figure S8). The activity of Ir-C6@Pt-TiO₂ was slightly lower than that of the simple mixture Pt-TiO₂ nanoparticles and Ir-C6 without immobilization (Figure S9), probably because the

electron donation from AA to the surface-immobilized Ir-C6 would occur more slowly than that to free Ir-C6 in the solution. Notably, the high activity of Ir-C6@Pt-TiO₂ was retained during two cycle reactions (Figure 6b), and the amounts of H₂ produced in both cycles were ~200 μmol. These results suggest that all the AA (0.02 M) was consumed as the two-electron donor for the H₂ evolution reaction. The absorption band derived from the surface-detached Ir-C6 was almost negligible in the UV-vis absorption spectra of the supernatant solution (Figure S10). Similar results were also obtained for Ir-C30@Pt-TiO₂ (Figure S11). These results clearly indicate that the performance of the Ir-CX@Pt-TiO₂ nanoparticle photocatalyst is superior.

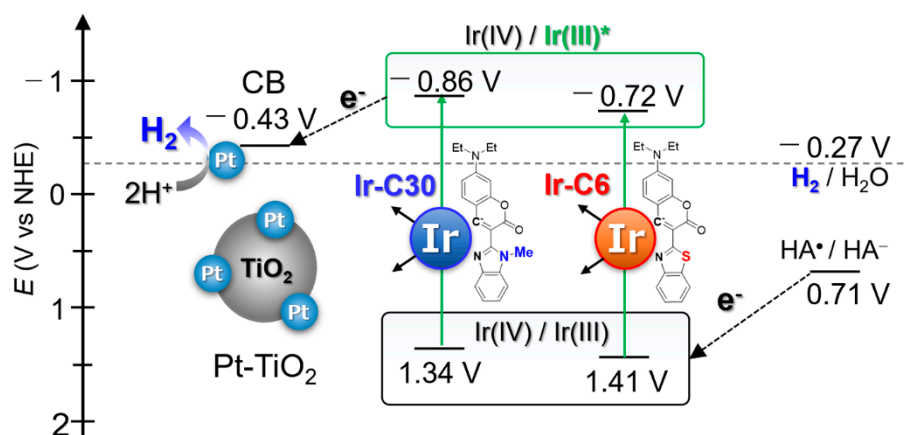


Figure 7. Schematic energy diagram showing the plausible mechanism of photocatalytic H₂ evolution reaction of Ir-CX@Pt-TiO₂ nanoparticles. The redox potential of one-proton released ascorbate anion (HA⁻) and the position of conduction band (CB) minimum of TiO₂ were inferred from the literatures [56,57].

4. Conclusions

In this work, two Ir(III)-coumarin complexes, Ir-C6 and Ir-C30, were synthesized as visible light photosensitizers, for the H₂ evolution reaction. UV-vis absorption and emission spectroscopy revealed that the LC absorption and emission bands of Ir-CX were blue-shifted by the replacement of the coumarin ligand from C6 to C30, whereas the LLCT transition energies estimated by TD-DFT calculations were comparable. These Ir-CX complexes were successfully immobilized on the surface of Pt-cocatalyst-loaded TiO₂ nanoparticles to form H₂-evolving Ir(III)-dye-sensitized photocatalysts with the general formula Ir-CX@Pt-TiO₂. Both photocatalysts were highly active toward H₂ evolution under irradiation of visible light ($\lambda > 420$ nm, TON: ~1300 for Ir-C6@Pt-TiO₂ and ~700 for Ir-C30@Pt-TiO₂ after 6 h irradiation) in the presence of 0.2 M L-AA electron donor aqueous solution. The AQYs of the H₂ evolution reaction under monochromatic light irradiation ($\lambda = 450 \pm 10$ nm) were comparable (2.3 and 2.1% for Ir-C6@Pt-TiO₂ and Ir-C30@Pt-TiO₂, respectively), owing to the comparable LLCT excited states, which are the key states for electron injection to TiO₂ nanoparticles. Thus, the superior performance of Ir-C6@Pt-TiO₂ for H₂ evolution over that of Ir-C30@Pt-TiO₂ under visible light originated from the wider and stronger light absorption ability of Ir-C6 ($\epsilon_{475} = 10.3 \times 10^4$) compared to that of Ir-C30 ($\epsilon_{452} = 6.76 \times 10^4$). Additionally, the energy difference between the LC and LLCT states of Ir-C6 may be sufficient for rapid internal conversion from the higher-lying LC to LLCT state. Further study on heteroleptic Ir(III) photosensitizers with intramolecular charge-separated LLCT states for solar water splitting is now in progress.

Supplementary Materials: The following are available online at <https://www.mdpi.com/article/10.3390/en14092425/s1>, Calculation of the amount of immobilized Ir(III) complexes on the Pt-TiO₂ nanoparticles and the surface coverage of Ir(III) complexes per unit area of TiO₂, Figure S1: PXRD pattern and TEM image of Pt-TiO₂ nanoparticles, Figure S2: UV-vis absorption spectra of the supernatant

solutions obtained from the immobilization reaction for Ir-C6@Pt-TiO₂ and Ir-C30@Pt-TiO₂ at 298 K, Figure S3: UV-vis absorption and emission spectra of C6 and C30, Figure S4: Emission decays of Ir-C6 and Ir-C30 in 12 μM MeOH/H₂O solution, Figure S5: Cyclic voltammograms of Ir-C30 and Ir-C6 immobilized on ITO working electrode, Figure S6: Estimated area occupied by one Ir-C30 molecule based on the X-ray structure, Figure S7: Photocatalytic H₂ evolution reaction under monochromatic light irradiation driven by the Pt-cocatalyst-loaded TiO₂ nanoparticles Ir-C6@Pt-TiO₂ and Ir-C30@Pt-TiO₂, Figure S8: Changes of UV-vis absorption and emission spectra of Ir-C30 by lowering pH from 10 to 4.5 in MeOH/H₂O mixed solvent at 298 K, Figure S9: Photocatalytic H₂ evolution reaction driven by the mixture of homogeneous Ir-C6 photosensitizer and Pt-TiO₂ nanoparticle, Figure S10: UV-vis absorption spectra of the supernatant solution obtained by centrifugation of the reaction solution of Ir-C6@Pt-TiO₂ after two cycles of 20 h photocatalytic H₂ evolution reactions, Figure S11: Two-cycle photocatalytic H₂ evolution reaction driven by Ir-C30@Pt-TiO₂, Table S1: Absorbance of each supernatant solution and the calculated C_B and M_i values, Table S2: Crystal parameters and refinement data for Ir-C30, Table S3: Selected bond lengths and angles of Ir-C30, Table S4: Cartesian coordinates of the optimized Ir-C6' and Ir-C30' complexes, Table S5: Photophysical data of C6 and C30 in comparison with Ir-C30 and Ir-C6 in the solution state, Table S6: Structural comparison of the X-ray structure of Ir-C30 and optimized structures Ir-C30' and Ir-C6' by DFT calculations, Tables S7 and S8: Energy, oscillator strength and major contribution of spin-allowed transitions for Ir-C30' and Ir-C6'.

Author Contributions: Conceptualization, A.K.; investigation, E.M.; resources, A.K. and M.K.; methodology, A.K.; formal analysis, and data curation E.M. and M.Y.; writing—original draft preparation, A.K.; writing—review and editing, M.K.; visualization, A.K.; supervision, M.K.; project administration, A.K.; funding acquisition, A.K. and M.K. All authors have read and agreed to the published version of the manuscript.

Funding: This study was supported by the ENEOS Hydrogen Trust Fund and JSPS KAKENHI, Grant Numbers JP18K19086, JP17H06367, and JP20H05082.

Institutional Review Board Statement: Not applicable.

Informed Consent Statement: Not applicable.

Data Availability Statement: Please refer to suggested Data Availability Statements in section “MDPI Research Data Policies” at <https://www.mdpi.com/ethics> (Accessed on 23 April 2021).

Acknowledgments: The authors would like to thank S. Takizawa (Univ. Tokyo) for the kind and helpful discussions about the syntheses and photocatalytic reactions of Ir(III)-coumarin complexes. The authors also thank J. Harada, M. Takehisa, Y. Kitagawa, and Y. Hasegawa for their kind helps for PXRD and TEM measurements.

Conflicts of Interest: The authors declare no conflict of interest.

References

1. Fujishima, A.; Honda, K. Electrochemical Photolysis of Water at a Semiconductor Electrode. *Nature* **1972**, *238*, 37–38. [[CrossRef](#)]
2. O'Regan, B.; Grätzel, M. A low-cost, high-efficiency solar cell based on dye-sensitized colloidal TiO₂ films. *Nature* **1991**, *353*, 737–740. [[CrossRef](#)]
3. Pelaez, M.; Nolan, N.T.; Pillai, S.C.; Seery, M.K.; Falaras, P.; Kontos, A.G.; Dunlop, P.S.M.; Hamilton, K.W.J.; Byrne, J.A.; O'Shea, K.; et al. A review on the visible light active titanium dioxide photocatalysts for environmental applications. *Appl. Catal. B* **2012**, *125*, 331–349. [[CrossRef](#)]
4. Zhang, X.; Peng, T.; Song, S. Recent advances in dye-sensitized semiconductor systems for photocatalytic hydrogen production. *J. Mater. Chem. A* **2016**, *4*, 2365–2402. [[CrossRef](#)]
5. Yuan, Y.-J.; Yu, Z.-T.; Chen, D.-Q.; Zou, Z.-G. Metal-complex chromophores for solar hydrogen generation. *Chem. Soc. Rev.* **2017**, *46*, 603–631. [[CrossRef](#)]
6. You, Y.; Nam, W. Photofunctional triplet excited states of cyclometalated Ir(III) complexes: Beyond electroluminescence. *Chem. Soc. Rev.* **2012**, *41*, 7061–7084. [[CrossRef](#)] [[PubMed](#)]
7. Mills, I.N.; Porras, J.A.; Bernhard, S. Judicious Design of Cationic, Cyclometalated Ir(III) Complexes for Photochemical Energy Conversion and Optoelectronics. *Acc. Chem. Res.* **2018**, *51*, 352–364. [[CrossRef](#)] [[PubMed](#)]
8. Goldsmith, J.I.; Hudson, W.R.; Lowry, M.S.; Anderson, T.H.; Bernhard, S. Discovery and High-Throughput Screening of Heteroleptic Iridium Complexes for Photoinduced Hydrogen Production. *J. Am. Chem. Soc.* **2005**, *127*, 7502–7510. [[CrossRef](#)]

9. Lowry, M.S.; Goldsmith, J.I.; Slinker, J.D.; Rohl, R.; Pascal, R.A.; Malliaras, G.G.; Bernhard, S. Single-layer electroluminescent devices and photoinduced hydrogen production from an ionic iridium(III) complex. *Chem. Mater.* **2005**, *17*, 5712–5719. [[CrossRef](#)]
10. Tinker, L.L.; McDaniel, N.D.; Curtin, P.N.; Smith, C.K.; Ireland, M.J.; Bernhard, S. Visible Light Induced Catalytic Water Reduction without an Electron Relay. *Chem. Eur. J.* **2007**, *13*, 8726–8732. [[CrossRef](#)]
11. Metz, S.; Bernhard, S. Robust photocatalytic water reduction with cyclometalated Ir(III) 4-vinyl-2,2'-bipyridine complexes. *Chem. Commun.* **2010**, *46*, 7551–7553. [[CrossRef](#)] [[PubMed](#)]
12. Wu, S.-H.; Ling, J.-W.; Lai, S.-H.; Huang, M.-J.; Cheng, C.H.; Chen, I.C. Dynamics of the Excited States of [Ir(ppy)2bpy]⁺ with Triple Phosphorescence. *J. Phys. Chem. A* **2010**, *114*, 10339–10344. [[CrossRef](#)] [[PubMed](#)]
13. Gärtner, F.; Cozzula, D.; Losse, S.; Boddien, A.; Anilkumar, G.; Junge, H.; Schulz, T.; Marquet, N.; Spannenberg, A.; Gladiali, S.; et al. Synthesis, Characterisation and Application of Iridium(III) Photosensitisers for Catalytic Water Reduction. *Chem. Eur. J.* **2011**, *17*, 6998–7006. [[CrossRef](#)]
14. Yuan, Y.-J.; Yu, Z.-T.; Chen, X.-Y.; Zhang, J.-Y.; Zou, Z.-G. Visible-Light-Driven H₂ Generation from Water and CO₂ Conversion by Using a Zwitterionic Cyclometalated Iridium(III) Complex. *Chem. Eur. J.* **2011**, *17*, 12891–12895. [[CrossRef](#)] [[PubMed](#)]
15. Yu, Z.-T.; Yuan, Y.-J.; Cai, J.-G.; Zou, Z.-G. Charge-neutral amidinate-containing iridium complexes capable of efficient photocatalytic water reduction. *Chem. Eur. J.* **2013**, *19*, 1303–1310. [[CrossRef](#)] [[PubMed](#)]
16. Neubauer, A.; Grell, G.; Friedrich, A.; Bokarev, S.I.; Schwarzbach, P.; Gärtner, F.; Surkus, A.-E.; Junge, H.; Beller, M.; Kühn, O.; et al. Electron- and Energy-Transfer Processes in a Photocatalytic System Based on an Ir(III)-Photosensitizer and an Iron Catalyst. *J. Phys. Chem. Lett.* **2014**, *5*, 1355–1360. [[CrossRef](#)]
17. Fan, S.; Zong, X.; Shaw, P.E.; Wang, X.; Geng, Y.; Smith, A.R.G.; Burn, P.L.; Wang, L.; Lo, S.-C. Energetic requirements of iridium(III) complex based photosensitisers in photocatalytic hydrogen generation. *Phys. Chem. Chem. Phys.* **2014**, *16*, 21577–21585. [[CrossRef](#)]
18. Kawashima, M.; Mori, K.; Aoyama, J.; Yamashita, H. Synthesis and Characterization of Ir and Rh Complexes Supported on Layered K₄Nb₆O₁₇ as a Heterogeneous Photocatalyst for Visible-Light-Induced Hydrogen Evolution. *Bull. Chem. Soc. Jpn.* **2014**, *87*, 874–881. [[CrossRef](#)]
19. Cai, J.-G.; Yu, Z.-T.; Yuan, Y.-J.; Li, F.; Zou, Z.-G. Dinuclear iridium(III) complexes containing bibenzimidazole and their application to water photoreduction. *ACS Catal.* **2014**, *4*, 1953–1963. [[CrossRef](#)]
20. Yuan, Y.-J.; Yu, Z.-T.; Liu, X.-J.; Cai, J.-G.; Guan, Z.-J.; Zou, Z.G. Hydrogen Photogeneration Promoted by Efficient Electron Transfer from Iridium Sensitizers to Colloidal MoS₂ Catalysts. *Sci. Rep.* **2014**, *4*, 4045. [[CrossRef](#)]
21. Paul, A.; Das, N.; Halpin, Y.; Vos, J.G.; Pryce, M.T. Carboxy derivatised Ir(III) complexes: Synthesis, electrochemistry, photophysical properties and photocatalytic hydrogen generation. *Dalton Trans.* **2015**, *44*, 10423–10430. [[CrossRef](#)] [[PubMed](#)]
22. Cheong, H.-Y.; Kim, S.-Y.; Cho, Y.-J.; Cho, D.W.; Kim, C.H.; Son, H.-J.; Pac, C.; Kang, S.O. Photosensitization Behavior of Ir(III) Complexes in Selective Reduction of CO₂ by Re(I)-Complex-Anchored TiO₂ Hybrid Catalyst. *Inorg. Chem.* **2017**, *56*, 12042–12053. [[CrossRef](#)]
23. Schönweiz, S.; Heiland, M.; Anjass, M.; Jacob, T.; Rau, S.; Streb, C. Experimental and Theoretical Investigation of the Light-Driven Hydrogen Evolution by Polyoxometalate-Photosensitizer Dyads. *Chem. Eur. J.* **2017**, *23*, 15370–15376. [[CrossRef](#)]
24. Torres, J.; Carrión, M.C.; Leal, J.; Jalón, F.A.; Cuevas, J.V.; Rodríguez, A.M.; Castañeda, G.; Manzano, B.R. Cationic bis(cyclometalated) Ir(III) complexes with pyridine–carbene ligands. Photophysical properties and photocatalytic hydrogen production from water. *Inorg. Chem.* **2018**, *57*, 970–984. [[CrossRef](#)]
25. Kobayashi, A.; Watanabe, S.; Yoshida, M.; Kato, M. Importance of the Molecular Orientation of an Iridium(III)-Heteroleptic Photosensitizer Immobilized on TiO₂ Nanoparticles. *ACS Appl. Energy Mater.* **2018**, *1*, 2882–2890. [[CrossRef](#)]
26. Bevernaegie, R.; Wehlin, S.A.M.; Piechota, E.J.; Abraham, M.; Philouze, C.; Meyer, G.J.; Elias, B.; Troian-Gautier, L. Improved visible light absorption of potent iridium(III) photo-oxidants for excited-state electron transfer chemistry. *J. Am. Chem. Soc.* **2020**, *142*, 2732–2737. [[CrossRef](#)]
27. Mayo, E.I.; Kilså, K.; Tirrell, T.; Djurovich, P.I.; Tamayo, A.; Thompson, M.E.; Lewis, N.S.; Gray, H.B. Cyclometalated iridium(III)-sensitized titanium dioxide solar cells. *Photochem. Photobiol. Sci.* **2006**, *5*, 871–873. [[CrossRef](#)]
28. Shinpuku, Y.; Inui, F.; Nakai, M.; Nakabayashi, Y. Synthesis and characterization of novel cyclometalated iridium(III) complexes for nanocrystalline TiO₂-based dye-sensitized solar cells. *J. Photochem. Photobiol. A* **2011**, *222*, 203–209. [[CrossRef](#)]
29. Gennari, M.; Légalité, F.; Zhang, L.; Pellegrin, Y.; Blart, E.; Fortage, J.; Brown, A.M.; Deronzier, A.; Collomb, M.-N.; Boujtita, M.; et al. Long-lived charge separated state in NiO-based p type dye sensitized solar cells with simple cyclometalated iridium complexes. *J. Phys. Chem. Lett.* **2014**, *5*, 2254–2258. [[CrossRef](#)] [[PubMed](#)]
30. Tschierlei, S.; Neubauer, A.; Rockstroh, N.; Karnahl, M.; Schwarzbach, P.; Junge, H.; Beller, M.; Lochbrunner, S. Ultrafast excited state dynamics of iridium(III) complexes and their changes upon immobilization onto titanium dioxide layers. *Phys. Chem. Chem. Phys.* **2016**, *18*, 10682–10687. [[CrossRef](#)] [[PubMed](#)]
31. Bobo, M.V.; Paul, A.; Robb, A.J.; Arcidiacono, A.M.; Smith, M.D.; Hanson, K.; Vannucci, A.K. Bis-Cyclometalated Iridium Complexes Containing 4,4'-Bis(phosphonomethyl)-2,2'-bipyridine Ligands: Photophysics, Electrochemistry, and High-Voltage Dye-Sensitized Solar Cells. *Inorg. Chem.* **2020**, *59*, 6351–6358. [[CrossRef](#)]
32. Takizawa, S.; Pérez-Bolívar, C.; Anzenbacher, P., Jr.; Murata, S. Cationic iridium complexes coordinated with coumarin dyes—Sensitizers for visible-light-driven hydrogen generation. *Eur. J. Inorg. Chem.* **2012**, *2012*, 3975–3979. [[CrossRef](#)]
33. Ma, L.; Guo, H.; Li, Q.; Guo, S.; Zhao, J. Visible light-harvesting cyclometalated Ir(III) complexes as triplet photosensitizers for triplet–triplet annihilation based upconversion. *Dalton Trans.* **2012**, *41*, 10680–10689. [[CrossRef](#)]

34. Yi, X.; Zhang, C.; Guo, S.; Ma, J.; Zhao, J. Strongly emissive long-lived³IL excited state of coumarins in cyclometalated Ir(III) complexes used as triplet photosensitizers and application in triplet–triplet annihilation upconversion. *Dalton Trans.* **2014**, *43*, 1672–1683. [[CrossRef](#)]
35. Happ, B.; Kübel, J.; Pfeffer, M.G.; Winter, A.; Hager, M.D.; Dietzek, B.; Rau, S.; Schubert, U.S. Towards Hydrogen Evolution Initiated by LED Light: 2-(1H-1,2,3-Triazol-4-yl)pyridine-Containing Polymers as Photocatalyst. *Macromol. Rapid Commun.* **2015**, *36*, 671–677. [[CrossRef](#)]
36. Sinopoli, A.; Wood, C.J.; Gibson, E.A.; Elliott, P.I.P. Hybrid Cyclometalated Iridium Coumarin Complex as a Sensitizer of Both n- and p-Type DSSCs. *Eur. J. Inorg. Chem.* **2016**, *2016*, 2887–2890. [[CrossRef](#)]
37. Takizawa, S.; Ikuta, N.; Zeng, F.; Komaru, S.; Sebata, S.; Murata, S. Impact of substituents on excited-state and photosensitizing properties in cationic iridium(III) complexes with ligands of coumarin 6. *Inorg. Chem.* **2016**, *55*, 8723–8735. [[CrossRef](#)] [[PubMed](#)]
38. Lu, Y.; Conway-Kenny, R.; Wang, J.; Cui, X.; Zhao, J.; Draper, S.M. Exploiting coumarin-6 as ancillary ligands in 1,10-phenanthroline Ir(III) complexes: Generating triplet photosensitizers with high upconversion capabilities. *Dalton Trans.* **2018**, *47*, 8585–8589. [[CrossRef](#)] [[PubMed](#)]
39. Sebata, S.; Takizawa, S.; Ikuta, N.; Murata, S. Photofunctions of iridium(III) complexes in vesicles: Long-lived excited states and visible-light sensitization for hydrogen evolution in aqueous solution. *Dalton Trans.* **2019**, *48*, 14914–14925. [[CrossRef](#)] [[PubMed](#)]
40. Wang, P.; Guo, S.; Wang, H.-J.; Chen, K.-K.; Zhang, N.; Zhang, Z.-M.; Lu, T.-B. A broadband and strong visible-light-absorbing photosensitizer boosts hydrogen evolution. *Nat. Comm.* **2019**, *10*, 3155. [[CrossRef](#)] [[PubMed](#)]
41. Park, H.; Choi, W.; Hoffmann, M.R. Effects of the preparation method of the ternary CdS/TiO₂/Pt hybrid photocatalysts on visible light-induced hydrogen production. *J. Mater. Chem.* **2008**, *18*, 2379–2385. [[CrossRef](#)]
42. Borisov, S.M.; Klimant, I. Ultrabright Oxygen Optodes Based on Cyclometalated Iridium(III) Coumarin Complexes. *Anal. Chem.* **2007**, *79*, 7501–7509. [[CrossRef](#)]
43. Norris, M.R.; Concepcion, J.J.; Glasson, C.R.K.; Fang, Z.; Lapides, A.M.; Ashford, D.L.; Templeton, J.L.; Meyer, T.J. Synthesis of phosphonic acid derivatized bipyridine ligands and their ruthenium complexes. *Inorg. Chem.* **2013**, *52*, 12492–12501. [[CrossRef](#)]
44. Furugori, S.; Kobayashi, A.; Watanabe, A.; Yoshida, M.; Kato, M. Impact of photosensitizing multilayered structure on ruthenium(II)-dye-sensitized TiO₂-nanoparticle photocatalysts. *ACS Omega* **2017**, *2*, 3901–3912. [[CrossRef](#)]
45. *CrysAlisPro*, Version 1.171.39.45h; Rigaku Corporation: Oxford, UK, 2018.
46. Sheldrick, G.M. A short history of SHELX. *Acta Crystallogr.* **2008**, *A64*, 112–122. [[CrossRef](#)]
47. Dolomanov, O.V.; Bourhis, L.J.; Gildea, R.J.; Howard, J.A.K.; Pushmann, H. OLEX2: A complete structure solution, refinement and analysis program. *J. Appl. Crystallogr.* **2009**, *42*, 339–341. [[CrossRef](#)]
48. Kiyota, J.; Yokoyama, J.; Yoshida, M.; Masaoka, S.; Sakai, K. Electrochemical O₂ evolution from water at an ITO electrode modified with [Ru(terpy){4,4'-(CH₂PO₃H₂)₂-2,2'-bpy}(OH₂)₂}²⁺: Evidence for a unimolecular pathway. *Chem. Lett.* **2010**, *39*, 1146–1148. [[CrossRef](#)]
49. Yanai, T.; Tew, D.P.; Handy, N.C. A new hybrid exchange–correlation functional using the Coulomb-attenuating method (CAM-B3LYP). *Chem. Phys. Lett.* **2004**, *393*, 51–57. [[CrossRef](#)]
50. Hehre, W.J.; Ditchfield, R.; Pople, J.A. Self-Consistent Molecular Orbital Methods. XII. Further Extensions of Gaussian-Type Basis Sets for Use in Molecular Orbital Studies of Organic Molecules. *J. Chem. Phys.* **1972**, *56*, 2257–2261. [[CrossRef](#)]
51. Andrae, D.; Häussermann, U.; Dolg, M.; Stoll, H.; Preuss, H. Energy-adjusted ab initio pseudopotentials for the second and third row transition elements. *Theor. Chim. Acta* **1990**, *77*, 123–141. [[CrossRef](#)]
52. Frisch, M.J.; Trucks, G.W.; Schlegel, H.B.; Scuseria, G.E.; Robb, M.A.; Cheeseman, J.R.; Scalmani, G.; Barone, V.; Mennucci, B.; Petersson, G.A.; et al. *Gaussian 09, Revision E.01*; Gaussian, Inc.: Wallingford, CT, USA, 2009.
53. Lee, C.; Yang, W.; Parr, R.G. Development of the Colle-Salvetti correlation-energy formula into a functional of the electron density. *Phys. Rev. B* **1988**, *37*, 785–789. [[CrossRef](#)] [[PubMed](#)]
54. Dennington, R.; Keith, T.; Millam, J. *GaussView 5.0*; Semichem Inc.: Shawnee Mission, KS, USA, 2009.
55. DeRosa, M.C.; Hodgson, D.J.; Enright, G.D.; Dawson, B.; Evans, C.E.B.; Crutchley, R.J. Iridium Luminophore Complexes for Unimolecular Oxygen Sensors. *J. Am. Chem. Soc.* **2004**, *126*, 7619–7626. [[CrossRef](#)] [[PubMed](#)]
56. Natali, M. Elucidating the Key Role of pH on Light-Driven Hydrogen Evolution by a Molecular Cobalt Catalyst. *ACS Catal.* **2017**, *7*, 1330–1339. [[CrossRef](#)]
57. Rothenberger, G.; Fitzmaurice, D.; Grätzel, M. Spectroscopy of Conduction Band Electrons in Transparent Metal Oxide Semiconductor Films: Optical Determination of the Flatband Potential of Colloidal Titanium Dioxide Films. *J. Phys. Chem.* **1992**, *96*, 5983–5988. [[CrossRef](#)]